Genetic stratigraphy, provenance, and new age constraints for the Chuska Sandstone (Upper Eocene-Lower Oligocene), New Mexico-Arizona

Steven M. Cather, Lisa Peters, Nelia W. Dunbar, and William C. McIntosh
2003, pp. 397-412. https://doi.org/10.56577/FFC-54.397

in:

Geology of the Zuni Plateau, Lucas, Spencer G.; Semken, Steven C.; Berglof, William; Ulmer-Scholle, Dana; [eds.], New Mexico Geological Society 54th Annual Fall Field Conference Guidebook, 425 p.
https://doi.org/10.56577/FFC-54

This page is intentionally left blank to maintain order of facing pages.

New Mexico Geological Society Guidebook, 54th Field Conference, Geology of the Zuni Plateau, 2003, p. 397-412.

GENETIC STRATIGRAPHY, PROVENANCE, AND NEW AGE CONSTRAINTS FOR THE CHUSKA SANDSTONE (UPPER EOCENE–LOWER OLIGOCENE), NEW MEXICO–ARIZONA

STEVEN M. CATHER, LISA PETERS, NELIA W. DUNBAR AND WILLIAM C. MCINTOSH
New Mexico Bureau of Geology and Mineral Resources, New Mexico Institute of Mining and Technology, Socorro, NM 87801

ABSTRACT.—The Chuska Sandstone is about 535 m thick and consists of a basal fluvial succession (Deza Member; 0–81 m thick) and overlying eolianites (Narbona Pass Member). Aggradation of the Deza Member occurred in response to the south–southwesterly progradation of the distal part of an extensive (200 km length) piedmont system derived from the San Juan uplift of southwestern Colorado. As it prograded, this system pushed ahead of it a short, northeast–facing piedmont system and a transverse basin-floor system as it onlapped a post-Laramide, late Eocene paleogeomorphic surface. Crossbedding in the eolianites of the Narbona Pass Member indicates paleowinds were mainly from the south–southwest, and blew up the paleoslope established during Deza Member deposition. The petrographic similarity of the Narbona Pass Member to the Deza Member indicates the eolianites are mostly recycled Deza-type sands that continued to be derived fluvially from sedimentary, volcanic, and basement terranes to the north–northeast during deposition of the Narbona Pass Member. Stratigraphic and topographic relationships in the Chuska Mountains suggest that nearly one km of middle Eocene–lower Oligocene strata were once present in the axial part of the San Juan Basin, but were subsequently eroded.

New $^{40}Ar/^{39}Ar$ results for volcanic ashes in the Deza Member (34.75 ± 0.20 Ma) and the lower Narbona Pass Member (33.33 ± 0.25 Ma) and for trachybasalts that disconformably overlie the Chuska Sandstone near Narbona Pass (24.83 ± 0.26, 24.97 ± 0.16, 25.05 ± 0.17, 25.24 ± 0.17 Ma) indicate the basal Chuska Sandstone is upper Eocene, and the upper part of the unit is lower Oligocene and possibly lower upper Oligocene. Our radioisotopic results indicate the switch from dominantly fluvial to dominantly eolian sedimentation in the central Colorado Plateau occurred between 34.75 and 33.31 Ma. Age constraints for the beginning of Chuska eolian deposition are broadly compatible with those for other eolian successions in the Colorado Plateau–Rocky Mountains area. The switchover from fluvial to eolian processes may be a response to major global cooling that occurred ~34 Ma.

INTRODUCTION

The Chuska Sandstone (Gregory, 1917) crops out in a northwest-trending belt of exposures that occupy the higher elevations of the Chuska Mountains of New Mexico and Arizona (Fig. 1). The reader is referred to Lucas and Cather (this guidebook) for a discussion of the general stratigraphy and the history of previous investigations of the Chuska Sandstone. In the present report, we focus on the genetic stratigraphy of the Chuska Sandstone, its provenance, and new constraints on its age. The significance of these new results relative to paleoclimate and the landscape evolution of northwestern New Mexico will also be discussed.

The Chuska Sandstone is as much as 535 m thick and is flat-lying and undeformed, except where it has been tilted by late Tertiary to Holocene landsliding. The basal contact of the Chuska Sandstone is a low-relief angular unconformity (Tsaile surface of Schmidt, 1991) that bevels Laramide structure along the eastern margin of the Defiance uplift at an elevation near 8000 ft (2440 m). The top of the Chuska Sandstone attains elevations of nearly 9600 ft (2925 m) near Roof Butte, and is locally disconformably overlain by late Oligocene tephra and lavas of the Navajo volcanic field.

GENETIC STRATIGRAPHY AND PALEOCURRENTS

Using the terminology of Lucas and Cather (this guidebook), the Chuska Sandstone consists of two members, the Deza Member and overlying Narbona Pass Member. The Deza Member is largely fluviatile and ranges from 0 to about 265 ft (0–81 m) thick. The basal contact of the Deza is an erosion surface that exhibits about 300 ft (100 m) of regional paleorelief (Lucas and Cather, this guidebook). The Deza Member appears to be thin or absent where

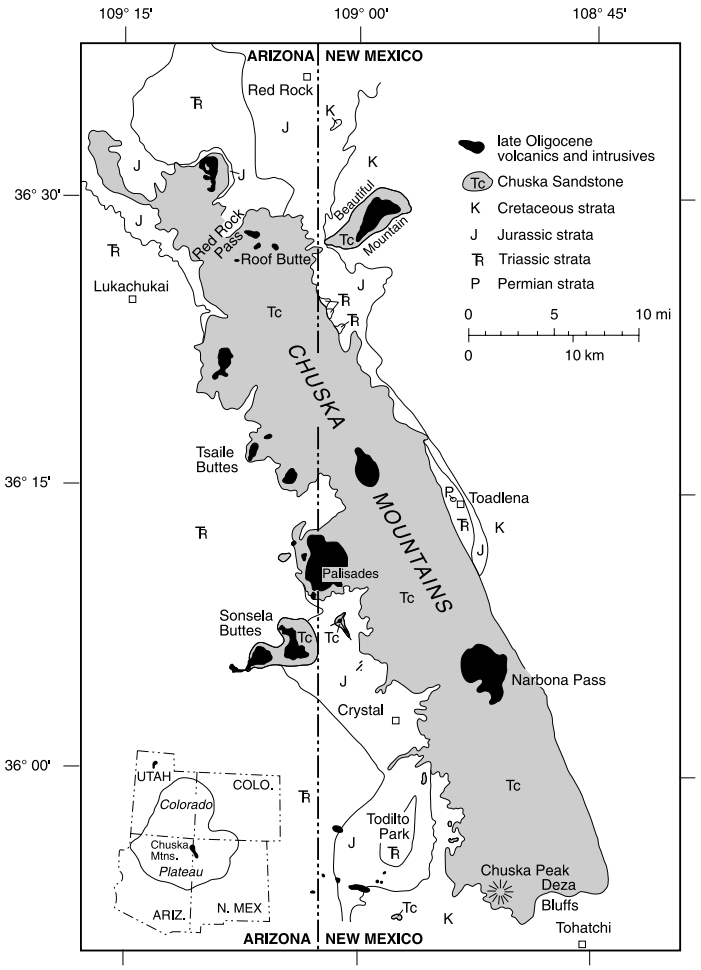

FIGURE 1. Geologic map of the Chuska Mountains showing the distribution of the Chuska Sandstone, Mesozoic rocks, and late Oligocene intrusive and extrusive rocks. Modified from Wright (1956).

the basal contact is at relatively high elevations, implying the Deza accumulated in broad, shallow paleovalleys that were carved into underlying Mesozoic strata. The Deza Member is conformably and transitionally overlain by the Narbona Pass Member.

Deza Member

Where it is best exposed at its type section near Deza Bluffs (Fig. 1) in the southern Chuska Mountains, the Deza Member is ~265 ft (~81 m) thick and consists mostly of poorly to moderately sorted fluvial sandstone and mudstone with subordinate lacustrine (pond) mudstone and minor eolian sandstone (Lucas and Cather, this guidebook). Impure limestone or marlstone has been described elsewhere in the Deza Member by Trevena (1979, his sample RW 1–1). At the type section, the Deza Member may be divided into three genetic stratigraphic components: (1) a thin, lower piedmont facies (fluvial), (2) an overlying basin-floor facies (fluvial, evaporitic pond, minor eolian), and (3) an upper piedmont facies (fluvial and minor eolian). Contacts between the three facies are conformable and gradational.

Lower piedmont facies

The lower piedmont facies encompasses the basal 7–10 m of the Deza Member (measured section units 1 and 2 of Wright, 1954; units 2 and 3 of Lucas and Cather, this guidebook). The base of the unit consists of channel-form pebbly sandstone 0.5–1.0 m thick that contains clasts predominantly of quartzite, chert, petrified wood, and well-indurated sandstone. Clasts are generally 0.5–8 cm in maximum diameter, but a few clasts as large as 18 cm were observed. Quartzite and chert clasts are well rounded and thus probably not of first-cycle derivation. The main part of the lower piedmont facies is composed of 7–9 m of mudstone and fine sandstone (unit 3 of Lucas and Cather, this guidebook) that transitionally overlies the basal pebbly sandstone and forms a prominent reddish-buff horizon at the type section (Fig. 2).

Sandstones in the lower piedmont facies exhibit upward-fining textures and trough crossbedding. Mudstone is generally structureless or indistinctly bedded, presumably due to bioturbation. Crossbedding shows that paleoflow during deposition of the lower piedmont facies was generally toward the northeast (Fig. 3a).

The lower piedmont facies is interpreted to have been deposited by bedload (mostly braided) streams. Aggradation occurred on a low-relief erosion surface that truncated folded Mesozoic strata (Fig. 4a). The lower piedmont facies was deposited as valley-fills and as short alluvial fans at the toe of a gentle northeast-facing paleoslope. Detritus was derived predominantly from Mesozoic strata exposed on the Defiance uplift nearby to the southwest (see regional map of Cather, this guidebook, fig. 1). Deposition occurred as northeast-flowing paleostreams on this erosion surface aggraded in response to the onlap of a large distal piedmont facies derived from the north–northeast (Figs. 4b, c; see description of upper piedmont facies).

Basin-floor facies

The basin-floor facies is 16–21 m thick and encompasses units 3–5 of the measured section of Wright (1954) and units 4–22 of Lucas and Cather (this guidebook). It consists dominantly of light-colored, horizontally stratified to structureless, very fine sandstone and sandy mudstone. Contorted bedding is common; crossbedding is rare. Veinlets of gypsum are locally present, rare sandstone bedding surfaces exhibiting mudcracks and poorly preserved cubic crystal casts (presumably halite) were noted in float. Bedding at the type section is thin and notably tabular (Fig. 2), with beds of decimeter-scale thickness persisting laterally in outcrop for many tens of meters. A few thin sandstone beds are anomalously well sorted and finely laminated, and possibly represent eolian sheet sands. Because of its fine-grained nature and rarity of crossbedding, paleocurrent directions for the basin-floor facies are indeterminate (Fig. 3b).

Bedding characteristics indicate deposition of the basin-floor facies occurred dominantly in a low-energy, low-gradient environment by sheet-flooding along shallow fluvial systems. Minor eolian sheet-sand deposition also may have occurred locally. Contorted bedding indicates that near-surface deposits were saturated. The presence of gypsum and halite(?) suggests evaporitic conditions existed, perhaps within floodplain ponds.

The basin-floor facies is interpreted to have been deposited in a low-gradient, fluvially dominated area between opposing piedmont systems (Fig. 4b, c). As will be emphasized below, the lack of evidence for deposits of a major, extrabasinal fluvial system in the basin-floor facies has important implications for the Paleogene landscape development of northwestern New Mexico.

Upper piedmont facies

The upper piedmont facies composes the majority of the Deza Member, and attains a thickness of about 50 m at the type section.

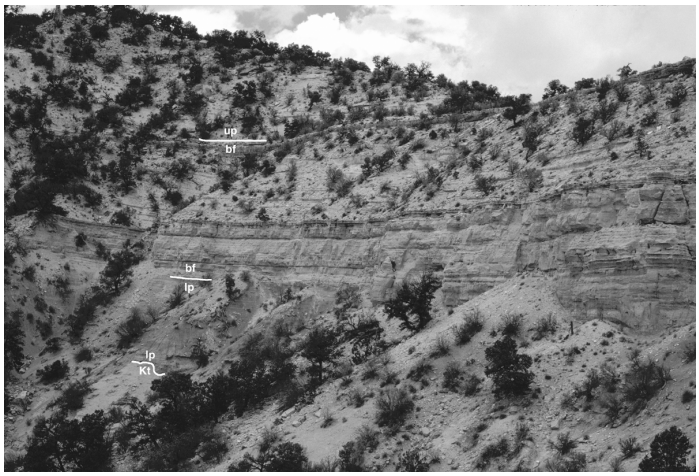

FIGURE 2. Photograph of type section of Deza Member of Chuska Sandstone near Deza Bluffs at southeast end of the Chuska Mountains. View is to the northwest. Contacts are shown for the lower piedmont facies (lp), basin-floor facies (bf) and the upper piedmont facies (up). Note the erosional unconformity at top of Cretaceous Tohatchi Formation (Kt) and the marked lateral continuity of beds in the basin-floor facies. Transitional contact between the upper piedmont facies and the overlying Narbona Pass Member is out of view to the upper left. Lower piedmont facies is 7–10 m thick; basin-floor facies is 16–21 m thick.

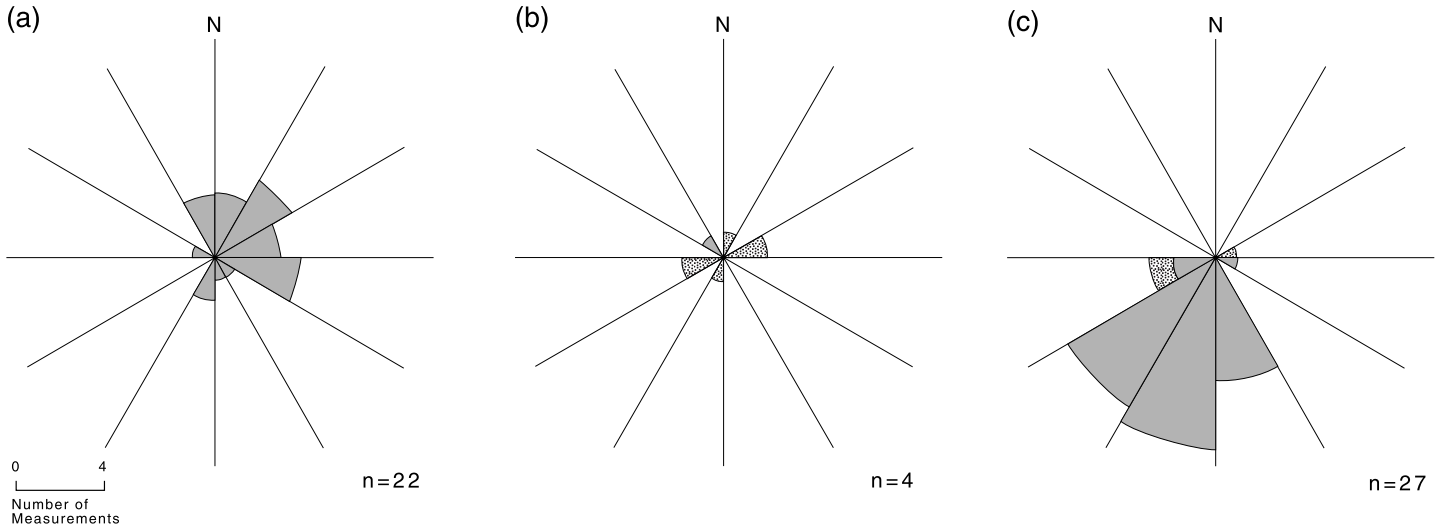

FIGURE 3. Paleocurrent rose diagrams for the Deza Member type section near Deza Bluffs. (a) lower piedmont facies; (b) basin-floor facies; (c) upper piedmont facies. Measurements represented by shading are unidirectional indicators (crossbedding, pebble imbrication). Measurements represented by stippled pattern are bidirectional indicators, mostly parting lineation.

Bedding is channel-form to tabular; very fine to medium sandstone and siltstone comprise the majority of the unit. Sandstones commonly display small- to medium-scale (0.1–0.5 m thick) trough crossbedding. Rhizoconcretions are present locally, and fossil turtle-shell fragments indicate the presence of perennial water during deposition of the upper piedmont facies (Lucas and Cather, this guidebook). A lenticular, 0–1.5 m thick bed of biotite-rich fallout ash is present near the base of the upper piedmont facies (unit 6 of Wright, 1954; unit 24 of Lucas and Cather, this guidebook) at the type section. This ash yielded a $^{40}Ar/^{39}Ar$ age of 34.75 ± 0.20 Ma (late Eocene; see geochronology section).

Paleocurrents were south–southwestward during deposition of the upper piedmont facies (Fig. 3c). In their analysis of the Deza Member, Repenning et al. (1958, p. 124) stated that "… most crossbeds are oriented in a 90-degree arc between southwest and southeast, indicating southerly flowing streams." Repenning et al. (1958), however, did not publish their paleocurrent data or state precisely the location of their measurements. Given the volumetric dominance of the upper piedmont facies within the Deza Member and the relatively abundant fluvial crossbedding within this facies, it is probable that the paleocurrent observations of Repenning et al. pertain to this unit.

The upper piedmont facies was deposited in the distal part of a broad, south-facing piedmont or alluvial slope system. The piedmont prograded southward in response to aggradation within constituent bedload (mostly braided) streams. Paleoflow within the upper piedmont system was approximately opposite that of the lower piedmont system (Fig. 3a, c). These opposing piedmonts were juxtaposed across a low gradient, transverse, basin-floor system. Onlap, driven by southward progradation of the upper piedmont system, produced the observed superposition of facies within the Deza Member (Fig. 4b, c).

Narbona Pass Member

As much as 535 m thick, the Narbona Pass Member constitutes the majority of the Chuska Sandstone. The Narbona Pass Member transitionally overlies the Deza Member and is characterized by well sorted, fine to very fine sandstone that commonly exhibits large scale (0.5 to 6 m) high angle (20°–30°) foreset crossbeds. These foresets are curved in plan view and bounded by broad, trough-shaped surfaces (Wright, 1956; Repenning et al., 1958), observations which led Wright (1956) to interpret the bedforms to have been eolian dunes of crescentic (barchan) shape. At the Deza type section, fluvial lithologies persist above the lowermost crossbedded eolian sandstone that is used to define the base of the Narbona Pass Member. The extent of interbedding of fluvial deposits with the eolianites of the middle and upper parts of the Narbona Pass Member, however, is unclear, primarily because most outcrops of the Narbona Pass Member are dominated by ledges of silica-cemented eolianites. Less-indurated deposits intervening between these ledges are rarely exposed. As described below, provenance data indicate that fluvial deposits petrographically similar to those of the upper piedmont facies may be present, albeit cryptically, throughout the Narbona Pass Member.

Previously undated, the Narbona Pass Member has yielded a $^{40}Ar/^{39}Ar$ age of 33.31 ± 0.25 Ma from an ash in its lower part, ~7.7 km west–northwest of Roof Butte (Fig. 1) (see geochronology section). The Narbona Pass Member is disconformably overlain by local lavas and tephra associated with the Navajo volcanic field (Appledorn and Wright, 1957; Semken, 2001). The contact between the Chuska Sandstone and the overlying volcanic rocks is an erosional surface with paleorelief of at least several tens of meters (Lucas and Cather, this guidebook). Regionally, rocks of the Navajo volcanic field have yielded late Oligocene–early Miocene K/Ar ages (~28–19 Ma; Semken, 2001). As will be described

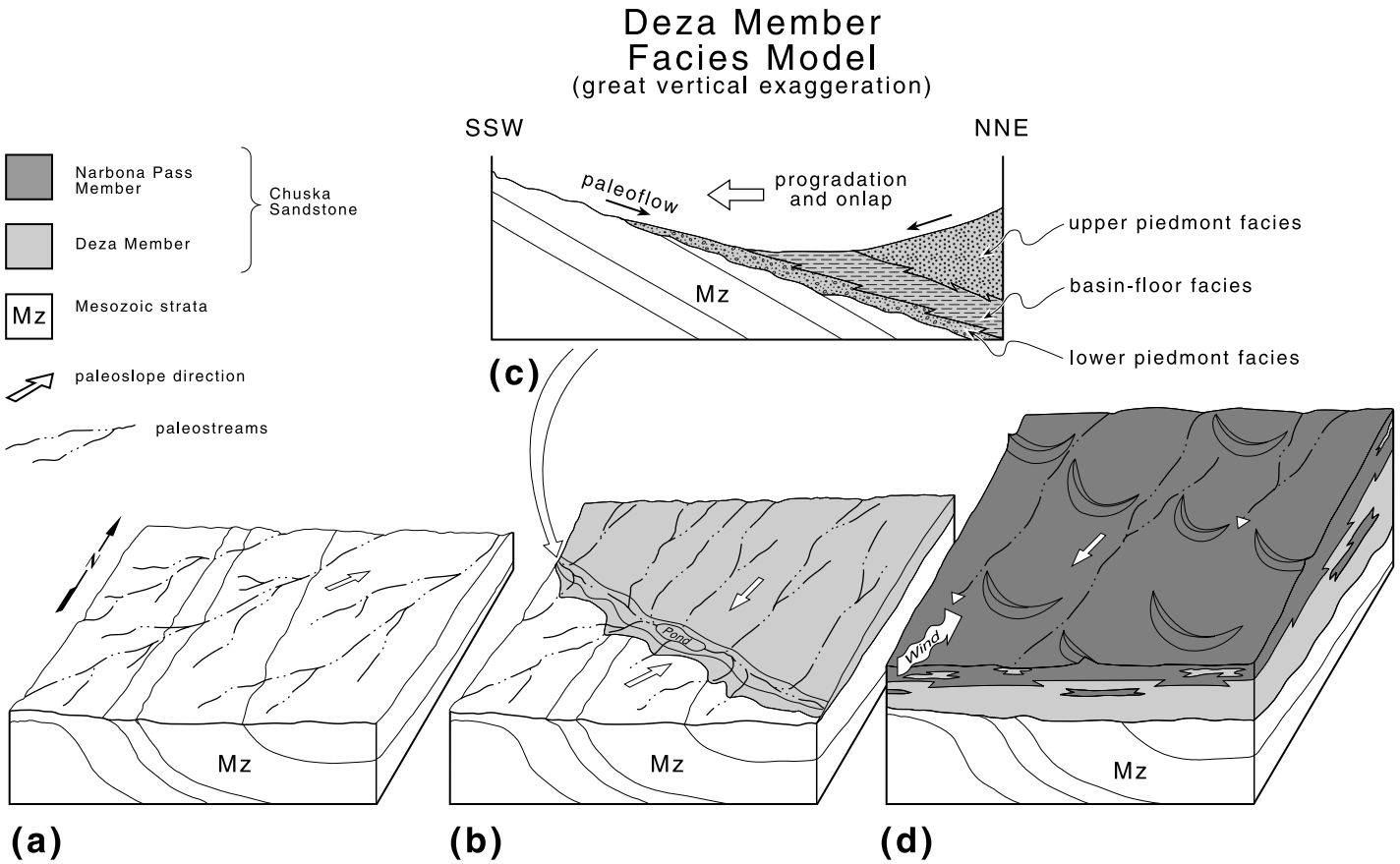

FIGURE 4. Block models showing interpretive depositional model for the Chuska Sandstone. (a) Low-relief paleogeomorphic surface of late Eocene age bevels Laramide structure along the Defiance monocline. Paleodrainage was northeastward, away from the structurally highest part of the Defiance uplift and toward the axial part of the San Juan Basin. (b) Deposition of the Deza Member (~35 Ma) is driven by the south–southwestward progradation of the distal part of an extensive piedmont system (upper piedmont facies) that drained the San Juan uplift to the north–northeast. Prograding piedmont pushes ahead of it a short, northeast-facing piedmont system (lower piedmont facies) and a transverse, basin-floor system (basin-floor facies). (c) Cross-section showing details of progradation and onlap of the Deza Member and resultant superposition of facies. Slopes are highly exaggerated for clarity. (d) Deposition of lower part of Narbona Pass Member (~33 Ma). Paleowinds from south–southwest cause eolian aggradation primarily resulting from deposition by barchan dunes that migrated up the prevailing south–southwest paleoslope. Eolian sands are recycled from Deza-type alluvium that continued to be supplied by streams from the San Juan uplift to the north–northeast. The onset of eolian sedimentation may be related to a ~34 Ma global cooling event (see text).

below, we have obtained new $^{40}Ar/^{39}Ar$ results that indicate a weighted mean age of 25.05 ± 0.16 Ma for maar-related trachybasalts that overlie the Chuska Sandstone near Narbona Pass.

Rigorous analysis of eolian crossbed orientation in the Narbona Pass Member was not undertaken in the present study. Previous studies of Narbona Pass Member crossbedding have interpreted a variety of paleowind directions, ranging from south–southeast to west. Wright (1956) measured the dip of several hundred crossbeds and concluded that paleowinds were from the south or southwest, averaging about S20°W. Based on 60 measurements of crossbeds, Trevena (1979) interpreted that paleowinds were from the south, ranging from south–southwest to south–southeast. In contrast, Repenning et al. (1958, p. 124) stated that "… most of the dips observed fall within a 45-degree arc between east and northeast, indicating winds from the west and southwest." Repenning et al., however, did not present their data or state from where their measurements were taken. Based on the combined crossbed data of Wright (1956) and Trevena (1979), the average paleowind direction during deposition of the Narbona Pass Member was from the south–southwest, an interpretation that is consonant with casual observations made during the present study. This indicates that paleowinds blew up the regional paleoslope established during deposition of the underlying, upper piedmont facies of the Deza Member (Figs. 3c, 4d). Eolian deposition is commonly induced by winds encountering rising topography (G. Kocurek, 2002, oral commun.), such as at the Great Sand Dunes National Monument in south-central Colorado.

PROVENANCE

The petrography of the Chuska Sandstone has been studied previously by Wright (1956) and Trevena (1979). Based on analyses of four samples, Wright (1956) determined the average detrital composition of the Chuska Sandstone to be 74% quartz, 23% feldspar, and 3% other. Wright noted the feldspar content of the Chuska Sandstone is higher than that of Jurassic and Cretaceous units in the region, which he nonetheless regarded as the most probable sources of Chuska detritus. Wright (1956) consid-

ered, but rejected, volcanic and basement terranes as sources for the Chuska Sandstone, primarily because he considered that the high roundness and sphericity of Chuska eolianite grains would require more than one cycle of erosion and transportation.

Trevena (1979) point-counted two thin sections from the Deza Member and four from the eolianites of the Narbona Pass Member. His results (Trevena, 1979, table 11) indicate the average QFR ratio for the Deza Member is 62:30:8 and the average QFR for the Narbona Pass Member is 55:35:10. Using the classification of Folk (1974), these sandstones are lithic arkose and arkose (Trevena, 1979, fig. 91). Although noting few volcanic rock fragments in thin section (0–8%, average <1%), Trevena (1979) and Trevena and Nash (1981) used microprobe data for feldspars to document substantial volcanic contributions to the Chuska Sandstone. Trevena (1979, p. 205) also considered the mineralogic immaturity of the Chuska Sandstone to indicate that most grains in the Chuska are first-cycle.

We sampled ten fine to very fine sandstones from the Chuska Sandstone for petrographic analysis. Three samples (one from each facies) were from the Deza Member at its type section near Deza Bluffs, three were from the Deza–lower Narbona Pass section about 1.6 km east of Crystal, New Mexico, and the remaining four were from the upper part of the Narbona Pass Member in its type area near Narbona (formerly Washington) Pass. The middle part of the Narbona Pass Member was not sampled. Thin sections were stained for K-feldspar and were point counted using standard petrographic techniques. A minimum of 300 points per section were counted. Abundances reported are percent of the framework (detrital) fraction.

The goal of our petrographic research is two-fold: first, to characterize the detrital sources of the Chuska Sandstone and, second, to evaluate any gross up-section changes in detrital composition that may be present. Examination of only ten thin sections, however, is clearly insufficient to detect any small-scale variability in detrital composition that may be present in the Chuska Sandstone.

Because we did not stain our thin sections for plagioclase, we could not detect untwinned plagioclase and therefore cannot quantitatively estimate QFR for most samples from the Chuska Sandstone. For two thin sections from the Narbona Pass Member, however, plagioclase abundance was estimated using a combination of microprobe x-ray mapping and backscattered electron imaging (see below). Average QFR for these two samples is 55:20:25 (arkosic litharenite). Plagioclase in these two samples accounts for one-third to one-half of total feldspar; most plagioclase is untwinned.

Quartz

Quartz is the most abundant detrital mineral in the Chuska Sandstone (50.3–83.4%, mean 65.9% of framework grains). The most prevalent type is common quartz (monocrystalline, nonundulose to slightly undulose quartz; Folk, 1974); polycrystalline undulose, monocrystalline undulose, and polycrystalline nonundulose quartz grains are subordinate. Rare volcanic quartz grains were noted, but recognition of such grains by their characteristic idiomorphic habit and embayed margins in the Narbona Pass Member is difficult because of eolian rounding of grains. Second-cycle quartz grains consist predominantly of common quartz grains that exhibit abraded syntaxial overgrowths that were inherited from older sandstones. Such grains account for 1–2% of framework grains in the Narbona Pass Member (Fig. 5) and 3.7 to 22.3% of grains in the Deza Member, where they are particularly abundant in the lower piedmont facies. The diminished abundance of recycled quartz in the Narbona Pass Member may be, in part, the result of abrasional removal of overgrowths in an eolian environment. Roundness and sphericity of grains is notably higher in the eolianites of the Narbona Pass Member than in the Deza Member.

Rock fragments

Rock fragments were present in all thin sections studied (10.8–34.5%, mean 19.3% of framework grains), and include a variety of metamorphic, sedimentary, plutonic, and volcanic types. For the purposes of provenance analysis and visualization of up-section changes, we apportioned lithic types into three categories: basement-derived, sedimentary-derived, and volcanic-derived. These three types are of approximately subequal average abundance in the Chuska Sandstone.

Basement rock fragments consist of both plutonic/gneissic (quartz + feldspar) and metamorphic lithics. Metamorphic lithics consist predominately of quartzitic (quartz + muscovite) and phyllitic types. There are no obvious up-section trends in abundance of basement-derived rock fragments in the Chuska Sandstone (Fig. 5).

Sedimentary rock fragments consist predominantly of mudstone lithics (siltstone, claystone) and chert. Sandstone rock fragments are rare, as might be expected in the fine to very fine sandstones we studied. (As noted above, individual recycled sand grains were counted as quartz.) Limestone lithics are rare. Sedimentary rock fragments decrease in abundance upsection in the Chuska Sandstone (Fig. 5). Most or all of this decrease, however, may be ascribed to the decreased abundance of mudstone lithics in the Narbona Pass Member, presumably resulting from attrition in the eolian environment.

Volcanic rock fragments

Volcanic lithics consist of vitric, felsitic, and trachytic types. Vitric types (commonly devitrified) are the most common, particularly in the Narbona Pass Member. With the exception of relatively low abundances in the lower piedmont facies of the Deza Member, no distinct up-section trends in abundance of volcanic rock fragments are apparent in the Chuska Sandstone (Fig. 5).

Microscopic identification of vitric volcanic grains in the Chuska Sandstone proved to be challenging. In many instances, volcanic fragments have been devitrified and squashed between more rigid framework grains, producing areas of detrital matrix that are difficult to distinguish from similarly deformed mudstone rock fragments. Classification of such labile grains is thus in many cases equivocal; the abundances of volcanic lithics depicted in Figure 5 may prove to be somewhat overstated.

Feldspar

Both alkali and plagioclase feldspar are present in the Chuska Sandstone. Because our thin sections were not stained for plagioclase, with the petrographic microscope we were only able to identify readily plagioclase that is twinned. Thus, with the

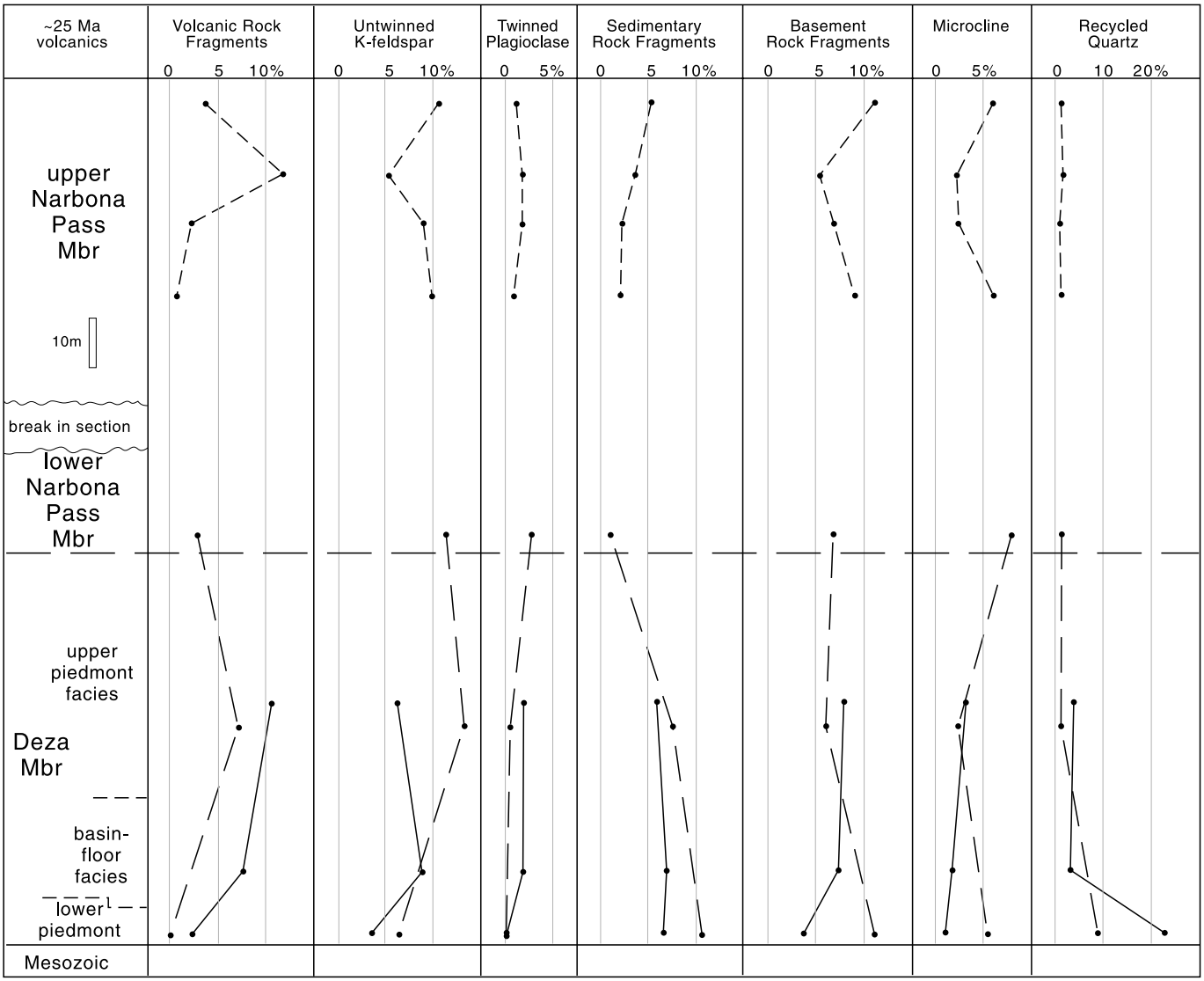

FIGURE 5. Up-section trends of abundance for detrital grains of diagnostic provenance in the Chuska Sandstone, based on point-count data for five thin sections from the Deza Member and five from the Narbona Pass Member. Solid line connects data points from Deza Member type section near Deza Bluffs (Fig. 1); long dashes connect data points from ~1.6 km east of Crystal, New Mexico; short dashes connect data points from near Narbona Pass. See text for discussion.

exception of two samples that were examined with the electron microprobe, we cannot quantify the amount of total feldspar or total plagioclase in our samples. Previous mean estimates for total feldspar range from 23% (Wright, 1956) to 33% (Trevena, 1979, table 11).

Using stained thin sections, point counting indicates the potassic feldspar content of the Chuska Sandstone ranges from 4.6–19.2%, and averages 12.2%. No obvious up-section trends in abundance of potassic feldspar are apparent. Potassic feldspar in the Chuska Sandstone consists of twinned (mostly microcline) and untwinned (mostly sanidine and orthoclase) crystals. We did not attempt to discriminate sanidine from orthoclase in this study, although at least part of the alkali feldspar in the Chuska Sandstone is of volcanic origin (Trevena, 1979). Untwinned potassic feldspar in the Chuska Sandstone shows no systematic up-section variation (Fig. 5). Because it is easily identified in thin section, we used abundances of twinned microcline as an additional tracer of basement sources of detritus in the Chuska Sandstone. Microcline also shows no systematic up-section variation in abundance (Fig. 5).

Plagioclase is present throughout the Chuska Sandstone, although much of it is untwinned (Trevena, 1979). Abundance of twinned plagioclase ranges from 0–3% (Fig. 5), whereas total plagioclase ranges from 9–19%, and averages 13.6% (Trevena, 1979, table 11). Trevena (1979, p. 245) used microprobe data to infer that at least 20% and possibly as much as 39% of the plagioclase in Chuska Sandstone is derived from intermediate to silicic volcanic rocks. This volcanic plagioclase is presumably mostly twinned, as untwinned plagioclase is rare or absent in volcanic rocks (D. Sawyer, P. Kyle, G. A. Smith, and C. E. Chapin, 2003, oral communications). The fraction of volcanic plagioclase in the Chuska, however, appears to be larger than the fraction of twinned

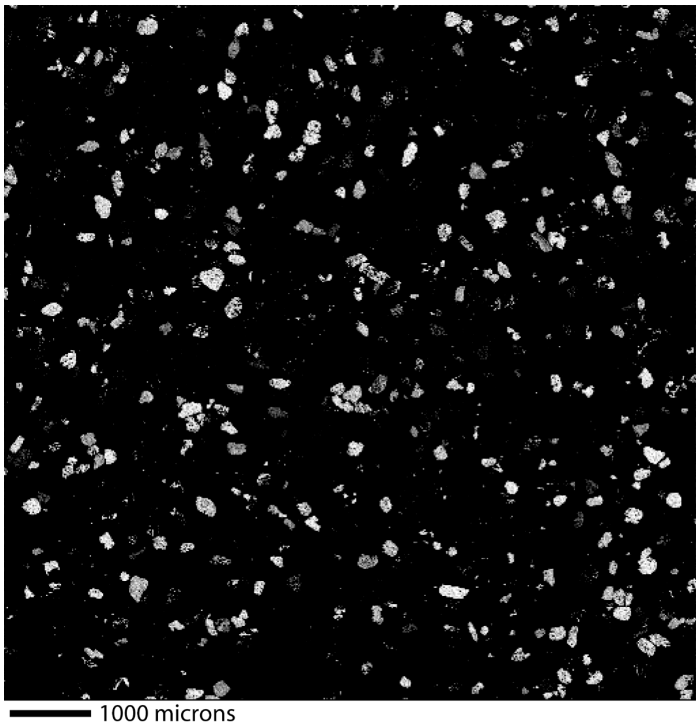

FIGURE 6. Sodium X-ray map of a polished thin section of sample Nar-3. The areas that appear bright are areas of significant Na concentration, typically plagioclase feldspar. The variations in brightness either within a single grain, or between grains, are indicative of differing Na concentrations in the imaged minerals.

plagioclase. This apparent discrepancy has not yet been resolved, although splitting of plagioclase grains along twin planes in an eolian environment may have been a factor. With the exception of possible diminished abundance in the lower piedmont facies of the Deza Member, twinned plagioclase shows no systematic up-section variation in abundance.

In order to measure the abundance and composition of plagioclase (twinned and untwinned) in the Chuska Sandstone, two polished thin sections were examined using a Cameca SX-100 electron microprobe. Samples examined (Nar-3 and Nar-4) are from the upper Narbona Pass Member near Narbona Pass. The samples were initially examined using backscattered electron imaging (BSE), but we found that it was difficult to distinguish between the sodic plagioclase and quartz due the similar mean atomic number of these two phases. Following this, we collected x-ray maps for elements Na and K in order to determine the amount of plagioclase present in the samples (Fig. 6). A test map for calcium was also collected, but proved less useful than the Na maps because of the presence of other Ca-bearing phases. Also, we observed that most plagioclase that contained Ca also contained detectable Na. However, it is possible that a small number of Ca-rich plagioclase grains were not detected by the Na maps. Two x-ray maps were collected per sample, each being 7.86 mm on a side, and imaging more than 1000 grains. The maps were acquired at a resolution of 512x512 pixels, with a 40 millisecond count time per pixel, accelerating voltage of 15 kV and probe current of 20 nA. Once the maps were acquired, each Na-bearing grain was checked in BSE in order to determine if it was a pure plagioclase grain or a rock fragment. Rock fragments, defined as any grain containing more than a single mineral phase, were manually erased from the image. In some cases, grains with a very small amount of K-feldspar in a dominantly plagioclase crystal were considered to be rock fragments, and were erased. These may or may not have been considered rock fragments during the petrographic point-counting process. The remaining grains were also compared to the K map, and K-rich feldspar grains were removed. Once the rock fragments and K-bearing feldspar grains were removed, the images were rendered into binary format, and the area percent of plagioclase was calculated for each using the freeware program ScionImage. Similar to the observations of Trevena (1979), we noted that many of the K-bearing feldspars in our samples were highly potassic. However, these grains were not analyzed quantitatively.

The area percent of plagioclase was calculated independently for each of the two images collected for each sample. The area percent based on the image was then corrected to area percent of framework fraction by removing the percent cement plus porosity determined by point counting. Sample Nar-3 appeared equigranular, and plagioclase was distributed relatively uniformly throughout the thin section. The area percent of plagioclase present in sample Nar-3 was 6.1% in one image, and 5.9% in the other. Once corrected for pre-cement porosity, these numbers become 10.1 and 9.8% of the framework fraction. The grain-size distribution of sample Nar-4 is more heterogeneous than that of Nar-3 and it also contains more rock fragments. The two maps collected from Nar-4 exhibit 3.4 and 4.4 area percent plagioclase, respectively, which, when corrected for pre-cement porosity, yields 5.0 and 6.4% of the framework fraction.

In addition to determining the percent plagioclase present in the samples, we also carried out quantitative analysis of 40 plagioclase grains per sample, selecting grains with a range of Na contents (based on the Na maps) in order to obtain a range of compositions. Plagioclase was analyzed for SiO_2, Na_2O, K_2O, CaO, FeO, Sr and Ba. The accelerating voltage used was 15 kV, probe current of 20 nA, and the beam was broadened to 10 μm in order to minimize Na volatilization. All elements were counted for 20 seconds, except for Sr and Ba, which were counted for 60. Standard ZAF recalculation procedures were used.

The quantitative analyses indicate that almost all of the grains that we had chosen based on the x-ray maps were plagioclase. A few alkali feldspars had also been picked as plagioclase, but not many (Fig. 7). The composition of the plagioclase is indistinguishable between the two samples, and tends to be albitic. The lack of any calcic plagioclase in the quantitative analyses suggests that we may have overlooked some plagioclase grains by focussing on the Na x-ray maps, but preliminary mapping for both Na and Ca suggested that calcic plagioclase grains are rare. Our results thus indicate plagioclase compositions and abundances that are broadly consistent with the estimates of Trevena (1979).

Provenance Summary

The Chuska Sandstone contains diagnostic grains that are indicative of ultimate derivation from basement (plutonic,

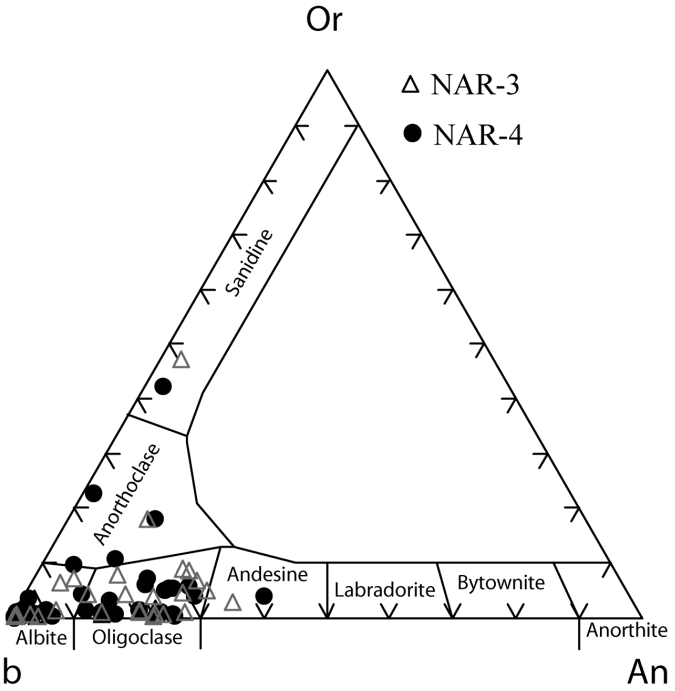

FIGURE 7. Feldspar ternary diagram of plagioclase feldspar crystals analyzed by electron microprobe. The analytical error is on the order of symbol size.

metamorphic), older sedimentary, and volcanic sources. With the exception of the lower piedmont facies of the Deza Member, no systematic up-section variation in the detrital character of the Chuska Sandstone is apparent (Fig. 5). The lower piedmont facies contains more quartz grains recycled from older sedimentary sources and less volcanic rock fragments and twinned plagioclase than the remainder of the Chuska Sandstone. These differences are consistent with derivation of the lower piedmont deposits predominantly from Mesozoic and possibly Permian sedimentary rocks on the Defiance uplift. Paleocurrents in the lower piedmont were northeastward, and point back toward potential sources on the structurally highest part of the Defiance uplift to the southwest. Because there were no basement rocks exposed during the late Eocene on the Defiance uplift (only tiny exposures of Proterozoic quartzite exist today), basement-derived detritus in the lower piedmont facies is probably recycled.

The majority of the Chuska Sandstone shows no significant up-section changes in provenance. This has also been noted by Trevena (1979, p. 245), who stated "… there was relatively little variation in the type of detritus supplied by the source terrain(s) during deposition of the Chuska." This observation has important implications for sediment dispersal patterns during Chuska deposition. If the main part of the Deza Member (the upper piedmont facies) and the eolianites of the Narbona Pass Member share the same source regions, then a continuance of Deza-style input of fluvial detritus from the north–northeast during Narbona Pass deposition is implied. Thus, although eolian deposition of the Narbona Pass Member was largely driven by winds from the south–southwest, these eolian processes were not importing sand from afar, but were simply recycling fluvial sediments that continued to be carried down the regional south–southwest paleoslope established previously during deposition of the underlying, upper piedmont facies. If correct, this hypothesis requires the presence of fluvial deposits locally throughout the Narbona Pass Member (Fig. 4d), although not necessarily those parts of the member that are preserved in the Chuska Mountains. Although fluvial deposits are present in lower part Narbona Pass Member where it intertongues with the Deza Member, no fluvial beds have been identified in the poorly exposed middle and upper parts of the eolian succession. Major southerly fluvial or eolian input of detritus to the Chuska Sandstone from the contemporaneous Spears Group (Cather, 1986; Chamberlin and Harris, 1994) and upper Mogollon Rim Formation (Potochnik and Faulds, 1998) can be ruled out on the basis of petrologic dissimilarity and probable paleogeographic isolation by the intervening Zuni and Defiance uplifts (Cather, this guidebook, fig. 1).

Paleocurrent data for the upper piedmont facies of the Deza Member point directly back toward the San Juan uplift ~200 km to the northeast (see Cather, this guidebook, fig. 1). Our provenance data are consistent with potential source lithologies in the San Juan uplift area, and no other source region seems to fit both the paleocurrent and provenance constraints. The San Juan uplift rose during the Laramide orogeny that ended shortly before the beginning of Chuska deposition. Exposures of older sedimentary strata and Proterozoic rocks were widespread on the uplift during the late Laramide, as shown by contact relationships beneath Oligocene volcanic rocks of the San Juan field (Lipman, 1989). Volcanic detritus in the Chuska Sandstone may have been derived from Laramide volcanic rocks associated with the southwestern part of the Colorado mineral belt (Cather, this guidebook, fig. 1) (~74–60 Ma; Mutschler et al., 1987; Semken and McIntosh, 1997) or from contemporaneous Conejos Formation volcanism in the San Juan volcanic field (34.7–31.1 Ma; Lipman et al., 1978). Additional volcanic detritus was contributed to the Chuska Sandstone by fallout ashes, two of which are dated below.

^{40}AR/^{39}AR GEOCHRONOLOGY

To help determine the timing of Chuska deposition, we used ^{40}Ar/^{39}Ar methods to date six samples. These included samples of two volcanic ash layers (one from the upper piedmont facies of the Deza Member and one from the lower part of the Narbona Pass Member) and four samples of maar-related trachybasalt lavas that disconformably overlie the Chuska Sandstone. We separated and dated sanidine and biotite from the Deza ash, biotite from the Narbona Pass ash, and concentrated groundmass from the trachybasalt samples. Separations were performed using standard crushing, sieving, ultrasonic cleaning, magnetic, density liquid, and hand picking methods. ^{40}Ar/^{39}Ar dating was performed at the New Mexico Geochronology Research Laboratory, using CO_2 laser-fusion and resistance-furnace step-heating methods similar to those detailed by McIntosh and Chamberlin (1994). Mineral separates and groundmass concentrates were irradiated in machined aluminum discs together with Fish Canyon Tuff sanidine as a neutron flux monitor (monitor age 27.84 Ma, equivalent to Mmhb-1 at 520.4 Ma, Samson and Alexander, 1987).

The sanidine and biotite from the two Chuska ashes were too fine-grained (typically < 150 μm diameter) to use single-crystal analytical methods to assess contamination. Microscopic examination of the lower ash indicated probable detrital contamination. Accordingly, we used laser fusion to analyze small multigrain aliquots (typically 20-30 grains per aliquot) of sanidine and biotite from the Deza ash. This approach does provide some assessment of contamination, although it is much less sensitive for this purpose than single-crystal analyses (Deino and Potts, 1990). Biotite from the Narbona Pass ash and biotite and groundmass concentrates from the overlying trachybasalts were analyzed using bulk-sample, resistance-furnace, step-heating methods. Results are summarized in Table 1, which also reports details of analytical parameters. Complete analytical data are provided in Appendix 1. Results from individual samples are summarized in Table 1, presented in Figures 8, 9, 10, and 11, and discussed below.

Initial laser fusion analyses of small 20–30 crystal aliquots of sanidine from the Deza ash (Fig. 8, Appendix 1) yielded widely scattered ages ranging from 39.1 to 377 Ma. We interpret these data as indicating that all of the analyzed aliquots represent

TABLE 1. Summary of $^{40}Ar/^{39}Ar$ results

Sample	Unit	Lab#	mineral	analysis	n	K/Ca	Age ±2σ (Ma)
Deza 2	Deza ash	53843	biotite	laser fusion	9	60.9	34.75 ± 0.20
Chuska 9	Narbona Pass ash	53778	biotite	furnace step heating	3	7.3	33.31 ± 0.25
Chuska 1	post-Chuska trachybasalt	53786	groundmass	furnace step heating	9	12.1	25.24 ± 0.17
Chuska 4	post-Chuska trachybasalt	53787	groundmass	furnace step heating	9	12.9	25.05 ± 0.17
Chuska 5	post-Chuska trachybasalt	53788	groundmass	furnace step heating	6	13.6	24.83 ± 0.26
Chuska 6	post-Chuska trachybasalt	53789	groundmass	furnace step heating	7	13.1	24.97 ± 0.16
mean	post-Chuska trachybasalts		groundmass				25.05 ± 0.16

Notes:
n is number of fusion aliquots or heating steps included in weighted-mean age calculation, K/Ca is calculated from measured ratio of 39ArK and 37ArCa.

Analytical parameters:

Sample preparation and irradiation:
Mineral separates were prepared by standard crushing, sieving, ultrasonic cleaning, magnetic, density liquid, and hand picking methods.
The separates were loaded into a machined Al disc and irradiated for 7 hours in D-3 position, Nuclear Science Center, College Station, TX.
Neutron flux monitor Fish Canyon Tuff sanidine (FCT-2). Assigned age = 27.84 Ma (Deino and Potts, 1990)
equivalent to Mmhb-1 at 520.4 Ma (Samson and Alexander, 1987).

Instrumentation:
Mass Analyzer Products 215-50 mass spectrometer on line with automated all-metal extraction system.
Deza-2 biotite analyzed by laser fusion of 20-30 crystal aliquots using a Synrad 50 watt CO2 laser.
Reactive gases removed during a 2 minute reaction with 2 SAES GP-50 getters, 1 operated at ~450°C and
1 at 20°C. Gas also exposed to a W filament operated at ~2000°C and a cold finger operated at -140°C.
Other samples step-heated in Mo double-vacuum resistance furnace, each step 7 minutes.
Reactive gases removed by reaction with 3 SAES GP-50 getters, 2 operated at ~450°C and
1 at 20°C. Gas also exposed to a W filament operated at ~2000°C.

Analytical parameters:
Electron multiplier sensitivity averaged $2.6x10^{-16}$ moles/pA and $1.5x10^{-16}$ moles/pA for the furnace and laser, respectively
Total furnace system blanks plus backgrounds were about:
4694,24.4, 3.4, 8.5, 15.4 x 10-18 moles at masses 40, 39, 38, 37, and 36, respectively for temperatures <1300°C.
Total laser system blanks plus backgrounds were about:
239, 2,2, 0.02, 2.9, 1.3 x 10-18 moles at masses 40, 39, 38, 37, and 36, respectively.
J-factors determined to a precision of ± 0.3% by CO_2 laser-fusion of 4 single crystals.
Correction factors for interfering nuclear reactions were determined using K-glass and CaF_2 and are as follows:
$(^{40}Ar/^{39}Ar)_K = 0.025\pm0.002$; $(^{36}Ar/^{37}Ar)_{Ca} = 0.00026\pm0.00002$; and $(^{39}Ar/^{37}Ar)_{Ca} = 0.00070\pm0.00005$.

Age calculations:
Total gas ages and errors calculated by weighting individual steps by the fraction of ^{39}Ar released. Plateau ages calculated by weighting each step by the inverse of the variance. Weighted mean ages for laser data calculated by weighting each age analysis by the inverse of the variance. All age errors calculated using the method of (Taylor, 1982). MSWD values are calculated for n-1 degrees of freedom for plateau and laser weighted mean ages. If the MSWD is outside the 95% confidence window (cf. Mahon, 1996; Table 1), the error is multiplied by the square root of the MSWD. Decay constants and isotopic abundances after Steiger and Jäger (1977). All final errors reported at ±2σ, unless otherwise noted.

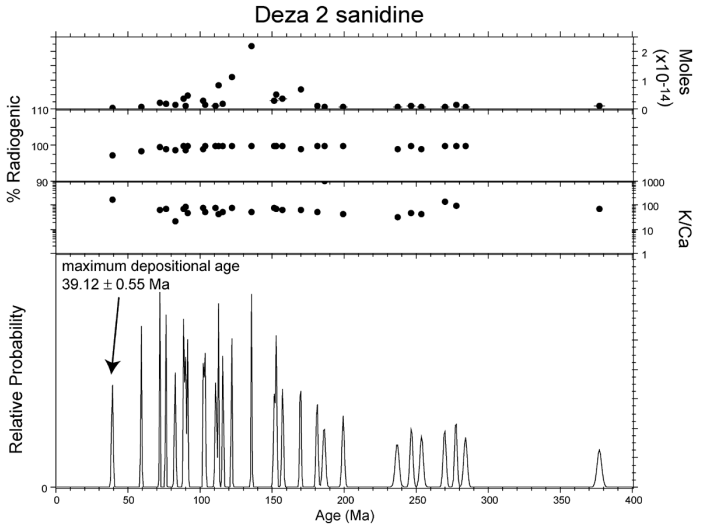

FIGURE 8. $^{40}Ar/^{39}Ar$ laser-fusion results from sanidine from ash layer in type section of Deza Member of the Chuska Formation. Sample location is 35°54.323'N, 108°45.579'W.

mixtures of phenocrystic sanidine and older detrital contaminant K-feldspar. Although these results provide a crude maximum age of 39.1 ± 1.1 Ma (all uncertainties quoted at 2 σ) for the Deza ash, the lack of a cluster of data at the lower end of the age range precludes interpretation of an eruption age from these data. Laser fusion results from small 20-30 crystal aliquots of biotite from the same samples range in age from 33.0 to 89.4 Ma (Fig. 9, Appendix 1). Like the sanidine results, these data are interpreted as indicating variable contamination by older detrital contaminant biotite. Unlike the sanidine, however, the ages of 8 of the 17 analyzed aliquots form a tight cluster near the young end of the age range (Fig. 9). These aliquots are interpreted as uncontaminated phenocrystic biotite, and their mean age (34.75 ± 0.20 Ma) is interpreted to be an accurate estimate of the eruption age of the Deza ash.

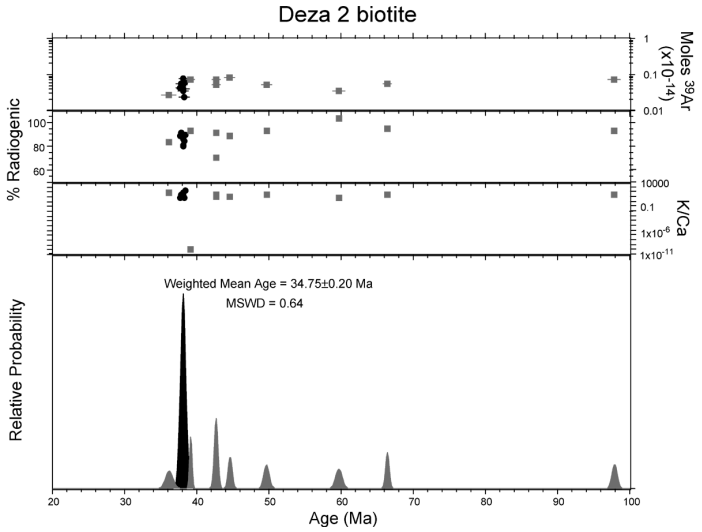

FIGURE 9. $^{40}Ar/^{39}Ar$ laser-fusion results from biotite from ash layer in Deza Member of the Chuska Formation. Sample location is same as Figure 8.

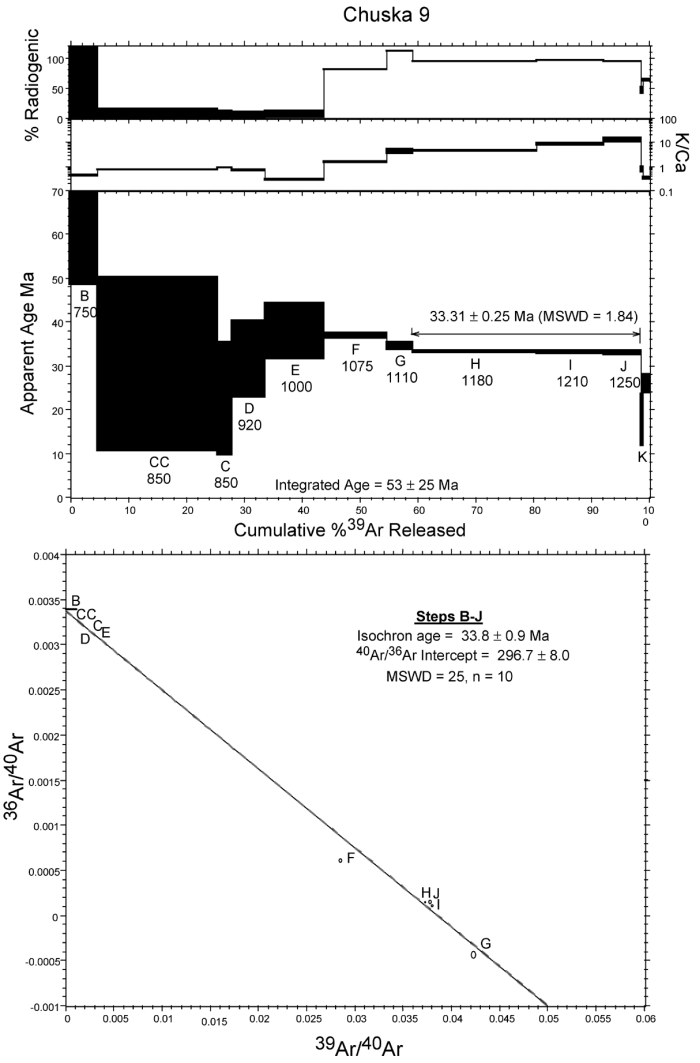

FIGURE 10. $^{40}Ar/^{39}Ar$ step-heating results from biotite from ash layer in the lower part of the Narbona Pass Member of the Chuska Formation. Sample location is E: 0663913 m, N: 4039768 m (UTM, zone 12S).

Step heating of bulk biotite from the ash in the Narbona Pass Member yielded a somewhat disturbed spectrum, apparently reflecting alteration of the biotite. Steps from the low-temperature half of the spectrum have low radiogenic yields, low K/Ca ratios (calculated from the ratio of measured $^{37}Ar_{Ca}$ to $^{39}Ar_{K}$), and variable, low-precision apparent ages (Figure 10, Appendix 2). These results are likely due to the presence of low-K alteration phases containing abundant atmospheric argon, which was released at low laboratory temperatures. Steps in the higher temperature half of the age spectrum, however, have much higher radiogenic yields, higher K/Ca ratios, and relatively precise, concordant ages. The average age of steps H, I , and J (33.31 ± 0.25 Ma) is considered to be the best available estimate of the eruption age of this ash, although, because of the evidence for alteration of the biotite, our confidence in the accuracy of this age is less than that for other samples dated in this study.

Age spectra from groundmass concentrates from all four samples of post-Chuska trachybasalt lavas are generally flat,

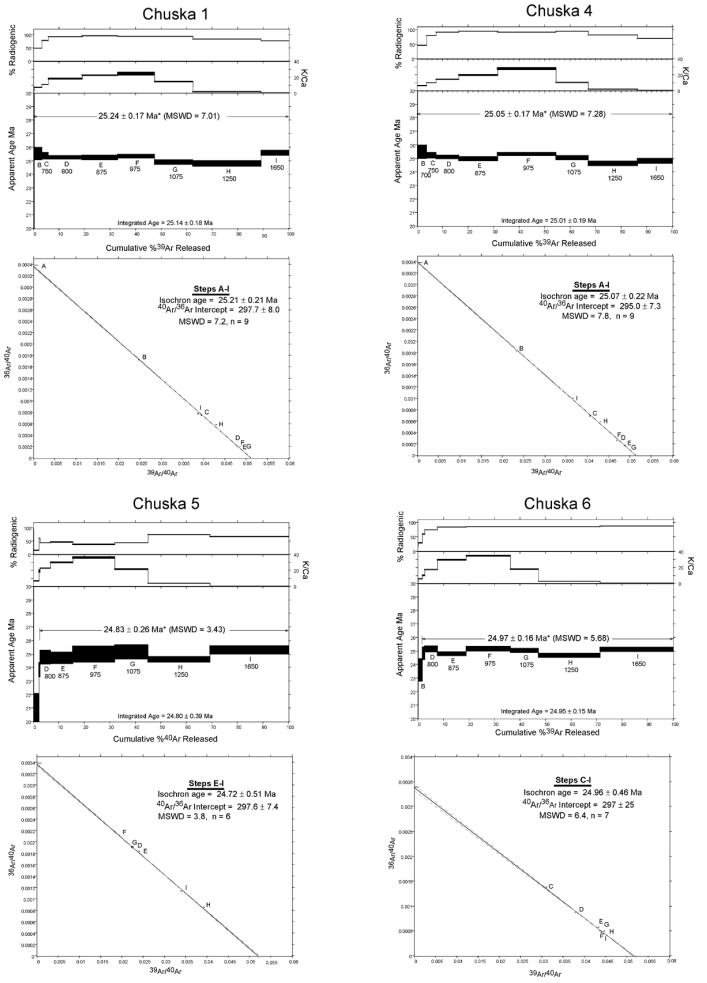

FIGURE 11. $^{40}Ar/^{39}Ar$ step-heating results from groundmass concentrates from mafic lavas overlying the Chuska Formation near Narbona Pass. Sample locations are: Chuska 1, 36°04.461'N, 108°53.349'W; Chuska 4, 36°06.331'N, 108°53.349'W; Chuska 5, 36°06.043'N, 108°53.057'W; Chuska 6, 36°05.302'N, 108°52.371'W.

with minor discordant steps at low and intermediate temperatures (Fig. 11, Appendix 2). These discordances probably reflect minor alteration and associated ^{39}Ar recoil artifacts in these fine-grained, polymineralic groundmass concentrates. Weighted-mean ages were calculated for these four samples, excluding only low-temperature discordant steps. The four weighted-mean ages all agree within analytical uncertainty, ranging from 24.83 ± 0.26 Ma to 25.24 ± 0.17 Ma (Fig.11, Table 1). Inverse isochron plots of these data yield statistically indistinguishable intercept ages, and trapped-component $^{40}Ar/^{36}Ar$ intercept values within error of atmospheric ratio ($^{40}Ar/^{36}Ar$ = 295.5). We interpret the weighted mean age of these four samples, 25.05 ± 0.16 Ma, to be an accurate estimate of their eruption age.

SUMMARY AND REGIONAL IMPLICATIONS

The Chuska Sandstone, now limited to exposures in or near the Chuska Mountains, represents only part of what initially must have been a much more widespread fluvial-eolian succession on the central Colorado Plateau. The Chuska Sandstone (~35–>25 Ma) is temporally equivalent to parts of major volcaniclastic aprons associated with the Mogollon–Datil volcanic field (Spears Group; Cather et al., 1994) and the San Juan volcanic field (Conejos Formation). About 200 km south of the Chuska Mountains, in the distal, northwestern part of the Mogollon–Datil field of southwestern New Mexico, major volcaniclastic eolianites are also present. These include the sandstone of Escondido Mountain (Chamberlin and Harris, 1994) and the upper sedimentary unit of Wrucke (1961). In west-central New Mexico, volcaniclastic eolian sedimentation began between the eruptions of the 34.2 Ma Rock House Canyon Tuff and the 32.1 Ma Hells Mesa Tuff and ended before eruption of the 26.1 Ma Bearwallow Mountain Andesite (Chamberlin and Harris, 1994; McIntosh and Chamberlin, 1994). Volcaniclastic eolianites of the sandstone of Escondido Mountain are best developed in the area south of Quemado, New Mexico, where they are as much as 240 m thick and consist almost exclusively of volcanogenic detritus (Chamberlin and Harris, 1994). Crossbedded eolian sandstones, probably equivalent to the sandstone of Escondido Mountain, crop out in east-central Arizona near Alpine and are as much as 360 m thick (Wrucke, 1961; Chamberlin and Harris, 1994). These eolianites, however, are not well dated.

The basal Chuska Sandstone (~35 Ma) was deposited on a low-relief paleoerosion surface, presently at ~8000 ft (2440 m) elevation, that post-dates the end of Laramide deformation in the Defiance monocline. This erosion surface is therefore almost certainly an approximate paleogeomorphic age-equivalent of the late Eocene erosion surface of Epis and Chapin (1975) in the Rampart Range of central Colorado, where a low-relief geomorphic surface post-dates Laramide deformation and is capped by the 36.7 Ma Wall Mountain Tuff.

Aggradation of the fluvial Deza Member was driven by the south–southwestward progradation of the distal part of an extensive (~200 km length) piedmont system or alluvial slope that drained the San Juan uplift of southwestern Colorado. As this piedmont onlapped the gently northeast-sloping late Eocene erosion surface, it pushed in front of it a short, northeast-facing piedmont system and an intervening, transverse, basin-floor system (Fig. 4c).

The lack of evidence for deposits of a major, extrabasinal fluvial system in the basin-floor facies of the Deza Member has important implications for the paleodrainage evolution of the San Juan Basin. During the Laramide orogeny, extrabasinal fluvial systems entered the subsiding San Juan Basin from many directions, but those entering the northwestern part of the basin near Farmington, New Mexico, were particularly long-lived. The first evidence of such a system is represented by the Farmington Sandstone Member of the Kirtland Formation (~74 Ma), which exhibits evidence for eastward paleoflow adjacent to the basin-bounding Hogback monocline near Farmington, New Mexico (Cather, this guidebook). The lower Paleocene Kimbeto Member of the Ojo Alamo Sandstone contains perhaps the best evidence for northwesterly fluvial input to the basin (Powell, 1973; Klute, 1986; Cather, this guidebook; Cather, in press). Sediment disper-

sal patterns of the Paleocene Nacimiento Formation have not been adequately studied, but paleocurrent data and evidence for thick, basin-axial fluvial sandstones in the overlying San Jose Formation indicate a component of fluvial input from northwest of the San Juan Basin during the early Eocene (Smith, 1988; Cather, 1992).

As shown by the sedimentological characteristics of the basin-floor facies of the Deza Member, major extrabasinal rivers had ceased entering the northwestern San Juan Basin by the late Eocene. Disruption of the long-lived pattern of fluvial input to the northwestern part of the basin occurred during the time interval between the deposition of the top of the San Jose Formation (~52 Ma; S. G. Lucas, oral commun., 2000) and the deposition of the basal Deza Member (~35 Ma). The stratigraphic record for this time interval is missing in the San Juan Basin, and encompasses the entire middle Eocene and parts of the lower and upper Eocene. Throughout many parts of the Rocky Mountain area, the late phase (Eocene) of Laramide deformation culminated during the middle Eocene, as shown by the tectonically induced hydrologic closure of many basins to form large lakes (e.g., Chapin and Cather, 1981, 1983). Most of these lakes developed ~52–47 Ma (Kester and Aase, 2002; Kester and Aase, unpublished stratigraphic chart), but strata of this age are not preserved in the San Juan Basin. It seems plausible that rapid middle Eocene tectonism was also responsible for the disruption of patterns of regional fluvial drainage adjacent to the San Juan Basin. Significant post-early Eocene tectonism undoubtedly occurred in the San Juan Basin, as the San Jose Formation is strongly folded along the north and east margins of the basin (e.g., Fassett, 1985). It is not known if middle Eocene tectonism produced lakes in the San Juan Basin, or simply beheaded drainages around the periphery of the basin as adjacent uplifts rose faster than rivers could incise through them. Clearly, however, the regional extrabasinal drainage network was greatly modified by late Eocene time. Following the cessation of Laramide subsidence in the San Juan Basin, piedmont deposits flanking the San Juan Uplift were able to prograde southward across the basin axis. Remnants of the distal part of these post-orogenic piedmont deposits in the southwestern part of the basin are now represented by the upper piedmont facies of the Deza Member.

The thickness of post-San Jose Formation sediments that have been subsequently stripped from the axial area of the San Juan Basin can be estimated approximately using stratigraphic data from the Chuska Mountains adjacent to the southwestern part of the basin. There, the base of the Chuska Sandstone is at ~8000 ft (2440 m) and the highest preserved beds are at nearly 9600 ft (2925 m) at Roof Butte. The highest beds of the San Jose Formation near the basin axis lie at about 6500 ft (1975 m). Based on the assumption that the top of the Chuska Sandstone was regionally extensive at about 9600 ft (2925 m) elevation, then the total thickness of the missing middle Eocene–lower Oligocene section near the basin axis is about 3100 ft (950 m). This estimate is reasonably close to the 2500 ft (760 m) value derived by Fassett (1985), who used somewhat different parameters to calculate the thickness of missing strata. If one neglects the effects of erosion-related isostatic rebound and the slight northeasterly regional dip of the basal contact of the Chuska Sandstone (as shown by paleocurrents) and if one assumes the top of the pre-Chuska deposits was just below the elevation of the base of the Chuska Sandstone, then the *maximum* thickness of the missing section of post-San Jose, pre-Chuska sediments near the basin axis was about 1500 ft (460 m). This thickness presumably represents mostly middle Eocene deposits and may approach that of the San Jose Formation (1800 ft; 550 m).

Regional ground-water tables must have risen to keep pace with aggradation of the Chuska Sandstone during the late Eocene and early Oligocene. Both the Deza and Narbona Pass members are loosely compacted and tightly cemented with early, phreatic cements. Neither member shows evidence of significant vadose cements. The principal cement in the Deza Member is sparry or poikilotopic calcite; meniscate or pendulose micritic cements characteristic of vadose diagenesis are rare. The dominant cements in the Narbona Pass Member are opal and chalcedony. In all samples examined, these siliceous cements exhibit early isopachous rims on detrital grains that are characteristic of phreatic diagenesis. Pre-cement porosity in the Chuska Sandstone is relatively high, indicating that little burial and compaction occurred prior to cementation. Pre-cement porosity ranges from 26.6–41.9% (mean 35.3%) for the Deza Member and 26.2–42.1% (mean 33.2%) for the Narbona Pass Member. The diagenetic characteristics of the Chuska Sandstone are indicative of early, shallow cementation in a phreatic environment, which in turn implies that ground water was relatively shallow throughout Chuska aggradation.

Radioisotopic ages from ashes closely constrain the transition from a dominantly fluviatile regime (Deza Member) to a dominantly eolian one to have occurred ~34 Ma, near the Eocene–Oligocene boundary. Our sample Deza-2 (34.75 ± 0.20 Ma) is from ~50 m below the fluvial/eolian transition in the southern part of the Chuska Mountains, whereas sample Chus-9 (33.31 ± 0.25 Ma) was collected ~85 m above the fluvial/eolian contact in the northern part of the range. The fluvial/eolian transition recorded by the base of the sandstone of Escondido Mountain in west-central New Mexico may have occurred at approximately the same time as that of the Chuska Sandstone, although the age brackets are broader (34.2–32.1 Ma; Chamberlin and Harris, 1994). The onset of eolian (loessic) sedimentation in the White River Formation of eastern Wyoming and vicinity also began at about this time (Evanoff et al., 1992; Obradovich et al., 1995), although it may have been regionally somewhat diachronous. Indeed, throughout the Colorado Plateau–Rocky Mountains region, except in proximal volcanic environments that continued to be dominated by fluvial and mass-flow processes, the time interval near the Eocene–Oligocene boundary seems to be marked by a switchover from fluvial to eolian regimes. Because the transition to an eolian regime was stratigraphically abrupt and approximately synchronous over a broad region, it was likely a response to climatic change. A major reorganization of global climate occurred at ~34 Ma, as shown by abrupt oceanic cooling of 2–3°C and the sudden, widespread glaciation of Antarctica (Zachos et al., 2001; Barrett, 2003; DeConto and Pollard, 2003). We suggest that the fluvial/eolian transition in the Chuska Sandstone and correlative strata is a response to this global climatic shift, possibly resulting from decreased vegetative stabilization of sediments in a colder and/or drier climate.

After accumulation of ~0.5 km of eolian sandstones, aggradation of the Chuska Sandstone ceased prior to ~25.05 Ma, the weighted mean age of the trachybasalts overlying the Chuska Sandstone at Narbona Pass. Significant erosional paleorelief at the top of the Chuska Sandstone indicates a period of erosion preceded late Oligocene volcanism, but the duration of this erosional episode is not well constrained. Post-Chuska erosion may mark the beginning of regional incision on the central Colorado Plateau. This erosional regime continued until the Bidahochi Formation began to aggrade in paleovalleys southwest of the Chuska Mountains about 16 Ma (Dallegge, 1999). The base of the Bidahochi Formation attains maximum elevations of about 7200 ft (2200 m) (Wright, 1956), ~2400 ft (730 m) below the top of the Chuska Sandstone.

ACKNOWLEDGMENTS

We benefited from discussions with S. G. Lucas, C. E. Chapin, E. Evanoff, R. M. Chamberlin, S. D. Connell and G. A. Smith. The paper was improved by reviews from C. E. Chapin, S. D. Connell, E. Evanoff, D. W. Love, and A. S. Trevena. We thank the Navajo Nation for access to tribal lands. Research was supported by the New Mexico Bureau of Geology and Mineral Resources (P. A. Scholle, Director). The manuscript was typed by Lynne Hemenway and the figures were drafted by Leo Gabaldon.

REFERENCES

Appledorn, C. R. and Wright, H. E., Jr., 1957, Volcanic structures in the Chuska Mountains, Navajo Reservation, Arizona–New Mexico: Geological Society of America Bulletin, v. 68, p. 445–468.

Barrett, P., 2003, Cooling a continent: Nature, v. 421, p. 221–223.

Cather, S. M., 1986, Volcano-sedimentary evolution and tectonic implications of the Datil Group (latest Eocene–early Oligocene), west-central New Mexico [Ph.D. dissertation]: Austin, University of Texas, 484 p.

Cather, S. M., 1992, Suggested revisions to the Tertiary tectonic history of north-central New Mexico: New Mexico Geological Society, Guidebook 43, p. 109–122.

Cather, S. M., this guidebook, Polyphase Laramide tectonism and sedimentation in the San Juan Basin, New Mexico.

Cather, S. M., in press, Laramide orogeny in central and northern New Mexico and southern Colorado, *in* Mack, G. H. and Giles, K., eds., The geology of New Mexico: New Mexico Geological Society, Special Publication.

Cather, S. M., Chamberlin, R. M., and Ratté, J. C., 1994, Tertiary stratigraphy and nomenclature for western New Mexico and eastern Arizona: New Mexico Geological Society, Guidebook 45, p. 259–266.

Chamberlin, R. M. and Harris, J. S., 1994, Upper Eocene and Oligocene volcaniclastic sedimentary stratigraphy of the Quemado–Escondido Mountain area, Catron County, New Mexico: New Mexico Geological Society, Guidebook 45, p. 269–275.

Chapin, C. E. and Cather, S. M., 1981, Eocene tectonics and sedimentation in the Colorado Plateau–Rocky Mountain area; *in* Dickinson, W. R. and Payne, W. D., eds., Relations of tectonics to ore deposits in the southern Cordillera: Arizona Geological Society Digest, v. 14, p. 173–198.

Chapin, C. E. and Cather, S. M., 1983, Eocene tectoncs and sedimentation in the Colorado Plateau, Rocky Mountain area; *in* Lowell, J. D., ed., Rocky Mountain foreland basins and uplifts: Denver, Rocky Mountain Association of Geologists, p. 33–56.

Dallegge, T. A., 1999, Correlation and chronology of the Miocene–Pliocene Bidahochi Formation, Navajo and Hopi Nations, northeastern Arizona [M.S. thesis]: Flagstaff, Northern Arizona University, 304 p.

DeConto, R. M. and Pollard, D., 2003, Rapid Cenozoic glaciation of Antarctica induced by declining atmospheric CO_2: Nature, v. 421, p. 245–249.

Deino, A., and Potts, R., 1990. Single-crystal $^{40}Ar/^{39}Ar$ dating of the Olorgesailie Formation, southern Kenya Rift: Journal of Geophysical Research, v. 95, p. 8453–8470.

Epis, R. C. and Chapin, C. E., 1975, Geomorphic and tectonic implications of the post-Laramide, late Eocene erosion surface in the southern Rocky Mountains: Geological Society of America, Memoir 144, p. 45–74.

Evanoff, E., Prothero, D. R., and Lander, R. H., 1992, Eocene–Oligocene climatic change in North America: the White River Formation near Douglas, east-central Wyoming; *in* Prothero, D. R. and Berggren, W. A., eds., Eocene–Oligocene climatic and biotic evolution: Princeton, Princeton University Press, p. 217–234.

Fassett, J. E., 1985. Early Tertiary paleogeography and paleotectonics of the San Juan Basin area, New Mexico and Colorado; *in* Flores, R. M. and Kaplan, S. S., eds.; Cenozoic paleogeography of the west-central United States: Denver, Rocky Mountain Section of the Society of Economic Paleontologists and Mineralogists, p. 317–334.

Folk, R. L., 1974, Petrology of sedimentary rocks: Austin, Hemphill Publishing Company.

Gregory, H. E., 1917, Geology of the Navajo country, a reconnaissance of parts of Arizona, New Mexico, and Utah: U.S. Geological Survey, Professional Paper 93, 161 p.

Kester, P. R. and Aase, A. K., 2002, Stratigraphic correlation of early Cenozoic intermontane lacustrine deposits of Wyoming, Colorado, and Utah: Geological Society of America, Abstracts with Programs, v. 34, no. 6, p. 558.

Klute, M. A., 1986, Sedimentology and sandstone petrography of the upper Kirtland Shale and Ojo Alamo Sandstone, Cretaceous–Tertiary boundary, western and southern San Juan Basin, New Mexico: American Journal of Science, v. 286, p. 463–488.

Lipman, P. W., Excursion 16B: Oligocene–Miocene San Juan volcanic field, Colorado; *in* Chapin, C. E. and Zidek, J., eds., Field excursions to volcanic terranes in the western United States, volume I: Southern Rocky Mountain region: New Mexico Bureau of Mines and Mineral Resources, Memoir 46, p. 303–380.

Lipman, P. W., Doe, B. R., Hedge, C. E., and Steven, T. A., 1978, Petrologic evolution of the San Juan volcanic field, southwestern Colorado: Pb and Sr isotope evidence: Geological Society of America Bulletin, v. 89, p. 59–82.

Lucas, S. G. and Cather, S. M., this guidebook, Stratigraphy of the Paleogene Chuska Sandstone, Arizona-New Mexico.

Mahon, K. I., 1996. The New "York" regression: Application of an improved statistical method to geochemistry: International Geological Review, v. 38, p. 293–303.

McDougall, I., and Harrison, T. M., 1999, Geochronology and thermochronology by the $^{40}Ar/^{39}Ar$ method: New York, Oxford University Press, xii, 269 p.

McIntosh, W. C. and Chamberlin, R. M., 1994, $^{40}Ar/^{39}Ar$ geochronology of middle to late Cenozoic ignimbrites, mafic lavas, and volcaniclastic rocks in the Quemado region, New Mexico: New Mexico Geological Society, Guidebook 45, p. 165–173.

Mutschler, F. E., Larson, E. E., and Bruce, R. M., 1987, Laramide and younger magmatism in Colorado—new petrologic and tectonic variations on old themes; *in* Drexler, J. W., and Larson, E. E., eds., Cenozoic volcanism in the southern Rocky Mountains updated: A tribute to Rudy C. Epis—Part 1: Golden, Colorado School of Mines Quarterly, v. 82, p. 1–47.

Obradovich, J. D., Evanoff, E., and Larson, E. E., 1995, Revised single-crystal laser-fusion $^{40}Ar/^{39}Ar$ ages of Chadronian tuffs in the White River Formation of Wyoming: Geological Society of America, Abstracts with Programs, v. 27, no. 3, p. 77–78.

Potochnik, A. R. and Faulds, J. E., 1998, A tale of two rivers: Tertiary structural inversion and drainage reversal across the southern boundary of the Colorado Plateau; *in* Duebendorfer, E. M., ed., Geologic excursions in northern and central Arizona: Geological Society of America, Field Trip Guidebook, p. 149–173.

Powell, J. W., 1973, Paleontology and sedimentation models of the Kimbeto Member of the Ojo Alamo Sandstone; *in* Fassett, J. E., Cretaceous and Tertiary rocks of the southern Colorado Plateau: Four Corners Geological Society Memoir, p. 111–122.

Repenning, C. A., Lance, J. F., and Irwin, J. H., 1958, Tertiary stratigraphy of the Navajo country: New Mexico Geological Society, Guidebook 9, p. 123–129.

Samson, S.D., and, Alexander, E.C., Jr., 1987. Calibration of the interlaboratory $^{40}Ar/^{39}Ar$ dating standard, Mmhb-1: Chemical Geology, v. 66, p. 27–34.

Schmidt, K.-H, 1991, Tertiary paleoclimatic history of the southeastern Colorado Plateau: Palaeogeography, Palaeoclimatology, Palaeoecology, v. 86, p. 282–296.

Semken, S. C., 2001, The Navajo volcanic field: New Mexico Museum of Natural History and Science, Bulletin 18, p. 79–83.

Semken, S. C. and McIntosh, W. C., 1997, $^{40}Ar/^{39}Ar$ age determinations for the Carrizozo Mountains laccolith, Navajo Nation, Arizona: New Mexico Geological Society, Guidebook 48, p. 75–80.

Smith, L. N., 1988, Basin analysis of the lower Eocene San Jose Formation, San Juan Basin, New Mexico and Colorado [Ph.D. dissertation]: Albuquerque, University of New Mexico, 166 p.

Steiger, R. H., and Jäger, E., 1977, Subcommission on geochronology: Convention on the use of decay constants in geo- and cosmochronology: Earth and Planetary Scientific Letters, v. 36, p. 359–362.

Taylor, J. R., 1982, An introduction to error analysis: The study of uncertainties in physical measurements: University Scientific Books, Mill Valley, California, 270 p.

Trevena, A. S., 1979 Studies in sandstone petrology: Origin of the Precambrian Mazatzal Quartzite and provenance of detrital feldspar [Ph.D. dissertation]: Salt Lake City, University of Utah, 316 p.

Trevena, A. S. and Nash, W. P., 1981, An electron microprobe study of detrital feldspar: Journal of Sedimentary Petrology, v. 51, p. 137–150.

Wright, H. E., Jr., 1954, Problem of the Tohatchi Formation, Chuska Mountains, Arizona–New Mexico: American Association of Petroleum Geologists Bulletin, v. 38, p. 1827–1834.

Wright, H. E., 1956, Origin of the Chuska Sandstone, Arizona–New Mexico: A structural and petrographic study of a Tertiary eolian sediment: Geological Society of America Bulletin, v. 67, p. 413–434.

Wrucke, C. T., 1961, Paleozoic and Cenozoic rocks in the Alpine–Nutrioso area, Apache County, Arzona: U.S. Geological Survey, Bulletin 1121–H, 26 p.

Zachos, J., Pagani, M., Sloan, L., Thomas, E., and Billups, K., 2001, Trends, rhythms, and aberrations in the global climate 65 Ma to present: Science, v. 292, p. 686–693.

Appendix 1. $^{40}Ar/^{39}Ar$ laser-fusion analytical data.

ID	$^{40}Ar/^{39}Ar$	$^{37}Ar/^{39}Ar$	$^{36}Ar/^{39}Ar$ (x 10^{-3})	$^{39}Ar_K$ (x 10^{-15} mol)	K/Ca	$^{40}Ar^*$ (%)	Age (Ma)	±1σ (Ma)
DEZA-2 san, M12:160, bulk san, J=0.0007217±0.11%, D=1.0052±0.00172, NM-160, Lab#=53798								
24	31.25	0.0032	2.958	0.177	161.8	97.2	39.12	0.55
25	47.03	-0.0016	2.676	0.286	-	98.3	59.22	0.36
32	56.70	0.0082	1.063	0.923	61.9	99.4	71.96	0.20
23	60.59	0.0071	2.636	0.677	72.0	98.7	76.24	0.27
05	66.02	0.0246	3.497	0.526	20.8	98.4	82.69	0.48
10	70.12	0.0075	1.013	1.480	68.3	99.6	88.70	0.32
16	71.74	0.0062	3.642	0.505	81.7	98.5	89.74	0.34
07	72.01	0.0105	0.3800	1.841	48.5	99.8	91.26	0.36
28	81.99	0.0069	3.534	1.230	73.8	98.7	102.43	0.25
27	82.00	0.0103	0.8229	0.510	49.4	99.7	103.43	0.41
34	88.23	0.0066	1.149	0.373	77.7	99.6	110.95	0.51
06	89.68	0.0115	0.9886	3.339	44.2	99.7	112.78	0.31
29	92.25	0.0099	0.9980	0.703	51.6	99.7	115.92	0.39
02	97.26	0.0069	1.232	4.454	73.4	99.6	121.94	0.33
01	108.5	0.0101	0.6931	8.824	50.3	99.8	135.73	0.30
09	121.7	0.0066	0.6259	1.103	76.9	99.8	151.62	0.60
04	122.8	0.0070	0.7788	2.047	72.7	99.8	152.97	0.40
08	126.7	0.0084	1.424	1.502	60.9	99.7	157.34	0.57
03	138.1	0.0078	4.995	2.744	65.7	98.9	169.66	0.48
31	146.8	0.0101	1.443	0.476	50.7	99.7	181.17	0.66
18	151.0	0.0005	1.543	0.260	982.1	99.7	186.09	0.95
30	162.2	0.0116	1.236	0.321	43.9	99.8	199.32	0.82
21	196.5	0.0166	7.427	0.239	30.8	98.9	236.8	1.3
20	203.4	0.0106	1.166	0.378	48.2	99.8	246.68	0.98
19	211.4	0.0124	7.391	0.362	41.3	99.0	253.7	1.2
33	224.2	0.0038	2.610	0.345	135.0	99.7	269.7	1.0
22	231.2	0.0052	2.597	0.621	97.6	99.7	277.52	0.86
26	237.3	-0.0011	2.894	0.345	-	99.6	284.2	1.2
17	381.5	0.0075	201.1	0.403	68.0	84.4	377.1	1.6
Mean age ± 2σ		n=29	MSWD=12077.45		100.3 ±344.7		108.2	16.9

Deza-2bi, D13:161, bulk bi, J=0.0006979±0.11%, D=1.00743±0.00124, NM-161, Lab#=53843								
09	*31.68*	*0.0081*	*17.66*	*0.352*	*62.9*	*83.5*	*33.02*	*0.48*
17	31.23	0.0695	12.40	0.594	7.3	88.3	34.39	0.24
11	30.55	0.0149	9.546	0.771	34.3	90.8	34.58	0.29
12	34.85	0.0064	23.54	0.542	79.4	80.0	34.78	0.42
02	31.37	0.0065	11.75	1.028	77.9	88.9	34.78	0.19
04	34.68	0.0358	22.96	0.713	14.3	80.4	34.79	0.24
18	32.50	0.0072	15.41	0.474	71.2	86.0	34.84	0.26
15	33.37	0.0954	18.15	0.325	5.3	83.9	34.93	0.38
10	31.40	0.0026	11.02	0.848	197.1	89.6	35.01	0.30
19	*30.87*	*-0.0009*	*7.437*	*0.947*	-	*92.9*	*35.74*	*0.16*
05	*44.07*	*0.0162*	*43.42*	*0.965*	*31.5*	*70.9*	*38.92*	*0.26*
16	*34.47*	*0.0411*	*10.82*	*0.705*	*12.4*	*90.7*	*38.96*	*0.21*
01	*36.89*	*0.0453*	*14.17*	*1.132*	*11.3*	*88.7*	*40.72*	*0.26*
13	*39.30*	*0.0222*	*9.644*	*0.698*	*22.9*	*92.8*	*45.31*	*0.35*
06	*42.45*	*0.0679*	*-4.9917*	*0.463*	*7.5*	*103.5*	*54.48*	*0.42*
20	*51.84*	*0.0161*	*9.697*	*0.731*	*31.8*	*94.5*	*60.63*	*0.23*
03	*78.36*	*0.0192*	*18.75*	*0.986*	*26.6*	*92.9*	*89.43*	*0.34*
Mean age ± 2σ		n=8	MSWD=0.64		60.9 ±126.8		34.75	0.20

Notes:
Isotopic ratios corrected for blank, radioactive decay, and mass discrimination, not corrected for interferring reactions. Ages calculated ralative to FC-1 Fish Canyon Tuff sanidine interlaboratory standard at 27.84 Ma. Errors quoted for individual analyses include analytical error only, without interferring reaction or J uncertainties. Mean age is weighted mean age of Taylor (1982). Mean age error is weighted error of the mean (Taylor, 1982), multiplied by the root of the MSWD where MSWD>1, and also incorporates uncertainty in J factors and irradiation correction uncertainties. Decay constants and isotopic abundances after Steiger and Jaeger (1977). # symbol preceding sample ID denotes analyses excluded from mean age calculations. Discrimination = 1.00743 ± 0.00124
Correction factors:
$(^{39}Ar/^{37}Ar)_{Ca}$ = 0.0007 ± 2e-05
$(^{36}Ar/^{37}Ar)_{Ca}$ = 0.00028 ± 5e-06
$(^{38}Ar/^{39}Ar)_{K}$ = 0.01077
$(^{40}Ar/^{39}Ar)_{K}$ = 0.0002 ± 0.0003

Appendix 2. $^{40}Ar/^{39}Ar$ furnace step-heating analytical data.

ID	Temp (°C)	$^{40}Ar/^{39}Ar$	$^{37}Ar/^{39}Ar$	$^{36}Ar/^{39}Ar$ (x 10^{-3})	$^{39}Ar_K$ (x 10^{-15} mol)	K/Ca	$^{40}Ar^*$ (%)	^{39}Ar (%)	Age (Ma)	±1σ (Ma)
Chus 9 biotite, 7.2 mg, J=0.0007278±0.11%, D=1.00743±0.00124, NM-160, Lab#=53778-01										
B	*750*	*25053.4*	*1.121*	*83613.8*	*1.78*	*0.46*	*1.4*	*4.9*	*405*	*178*
CC	*850*	*1497.8*	*0.6903*	*4993.4*	*7.39*	*0.74*	*1.5*	*25.4*	*30.6*	*9.9*
C	*850*	*731.2*	*0.5505*	*2416.3*	*0.90*	*0.93*	*2.4*	*27.9*	*22.6*	*6.4*
D	*920*	*551.8*	*0.7251*	*1785.2*	*2.05*	*0.70*	*4.4*	*33.6*	*31.7*	*4.4*
E	*1000*	*370.3*	*1.722*	*1154.4*	*3.69*	*0.30*	*7.9*	*43.9*	*38.1*	*3.2*
F	*1075*	*34.91*	*0.3265*	*21.96*	*3.91*	*1.6*	*81.5*	*54.7*	*36.98*	*0.26*
G	*1110*	*23.73*	*0.1160*	*-9.8524*	*1.60*	*4.4*	*112.3*	*59.2*	*34.66*	*0.38*
H	1180	26.85	0.1111	3.870	7.7	4.6	95.8	80.5	33.46	0.12
I	1210	26.35	0.0567	2.938	4.16	9.0	96.7	92.0	33.16	0.16
J	1250	26.64	0.0389	4.204	2.32	13.1	95.4	98.4	33.05	0.24
K	*1300*	*28.93*	*0.6426*	*52.17*	*0.127*	*0.79*	*46.9*	*98.8*	*17.7*	*3.0*
L	*1650*	*31.06*	*1.467*	*38.03*	*0.434*	*0.35*	*64.2*	*100.0*	*26.0*	*1.1*
Integrated age ± 2σ			n=12		36.1				53.1	25.1
Plateau ± 2σ		steps H-J	n=3	MSWD=1.84	14.2	7.3		39.3	33.31	0.25
Chus 1 groundmass, 47.7 mg, J=0.0007194±0.11%, D=1.00743±0.00124, NM-160, Lab#=53786-01										
A	625	1927.0	0.1737	6457.0	1.12	2.9	1.0	0.2	24.4	14.8
B	700	40.50	0.0717	70.05	17.7	7.1	48.9	3.4	25.52	0.23
C	750	25.34	0.0482	19.15	13.7	10.6	77.7	5.9	25.37	0.12
D	800	21.37	0.0280	5.986	73.3	18.2	91.7	19.1	25.265	0.061
E	875	20.72	0.0227	3.854	76.2	22.5	94.5	32.9	25.235	0.087

F	975	20.90	0.0210	4.200	80.5	24.3	94.1	47.4	25.345	0.066
G	1075	20.58	0.0362	4.301	83.3	14.1	93.8	62.5	24.897	0.081
H	1250	23.30	0.2992	13.82	147.9	1.7	82.6	89.2	24.81	0.11
I	1650	25.79	2.959	21.04	60.0	0.17	76.8	100.0	25.592	0.089
Integrated age ± 2σ			n=9		553.8				25.14	0.18
Plateau ± 2σ		steps A-I	n=9	MSWD=7.01	553.8	12.1		100.0	25.24	0.17
Chus 4 groundmass, 46.1 mg, J=0.0007181±0.11%, D=1.00743±0.00124, NM-160, Lab#=53787-01										
A	625	5584.7	0.3365	18832.0	0.561	1.5	0.4	0.1	25.5	39.2
B	700	42.99	0.0787	78.49	21.1	6.5	46.1	3.7	25.48	0.24
C	750	24.68	0.0518	17.15	21.5	9.8	79.5	7.3	25.24	0.10
D	800	21.30	0.0353	6.051	53.3	14.5	91.6	16.4	25.103	0.074
E	875	20.50	0.0260	3.645	88.7	19.6	94.8	31.5	24.992	0.075
F	975	21.33	0.0185	5.579	134.4	27.5	92.3	54.3	25.317	0.064
G	1075	20.52	0.0493	3.571	74.6	10.3	94.9	67.0	25.049	0.082
H	1250	23.23	0.2341	13.94	114.3	2.2	82.4	86.4	24.621	0.082
I	1650	27.32	2.245	27.90	79.9	0.23	70.5	100.0	24.819	0.098
Integrated age ± 2σ			n=9		588.2				25.01	0.19
Plateau ± 2σ		steps A-I	n=9	MSWD=7.28	588.2	12.9		100.0	25.05	0.17
Chus 5 groundmass, 52.7 mg, J=0.0007176±0.11%, D=1.00743±0.00124, NM-160, Lab#=53788-01										
A	*625*	*8051.6*	*0.2679*	*27501.5*	*0.488*	*1.9*	*-0.9*	*0.1*	*-99.9*	*66.2*
B	*700*	*101.3*	*0.0742*	*288.1*	*14.0*	*6.9*	*15.9*	*2.2*	*20.78*	*0.64*
C	*750*	*30.43*	*0.0266*	*40.23*	*3.39*	*19.2*	*60.9*	*2.7*	*23.84*	*0.27*
D	800	44.34	0.0224	84.90	27.1	22.8	43.4	6.7	24.76	0.26
E	875	41.58	0.0171	75.66	58.4	29.9	46.2	15.4	24.72	0.21
F	975	51.54	0.0142	108.7	110.9	36.0	37.7	31.9	24.98	0.29
G	1075	45.06	0.0239	86.31	87.7	21.4	43.4	44.9	25.15	0.25
H	1250	25.44	0.1460	21.41	163.0	3.5	75.2	69.2	24.60	0.10
I	1650	29.46	1.471	33.57	207.5	0.35	66.7	100.0	25.31	0.15
Integrated age ± 2σ			n=9		672.5				24.80	0.39
Plateau ± 2σ		steps D-I	n=6	MSWD=3.43	654.7	13.6		97.3	24.83	0.26
Chus 6 groundmass, 41.8 mg, J=0.0007184±0.11%, D=1.00743±0.00124, NM-160, Lab#=53789-01										
A	*625*	*1186.1*	*0.3147*	*3960.6*	*0.737*	*1.6*	*1.3*	*0.1*	*20.3*	*9.8*
B	*700*	*60.11*	*0.0884*	*141.4*	*8.4*	*5.8*	*30.5*	*1.6*	*23.60*	*0.42*
C	750	32.34	0.0519	44.15	5.81	9.8	59.7	2.7	24.84	0.23
D	800	26.36	0.0296	23.07	27.3	17.3	74.1	7.5	25.16	0.11
E	875	23.01	0.0174	12.66	63.5	29.3	83.7	18.8	24.805	0.071
F	975	22.80	0.0147	10.99	97.5	34.7	85.8	36.2	25.169	0.084
G	1075	22.87	0.0288	11.52	61.7	17.7	85.1	47.2	25.057	0.074
H	1250	22.44	0.2175	11.11	135.1	2.3	85.4	71.3	24.677	0.078
I	1650	22.46	1.190	10.32	161.0	0.43	86.9	100.0	25.128	0.076
Integrated age ± 2σ			n=9		560.9				24.95	0.15
Plateau ± 2σ		steps C-I	n=7	MSWD=5.68	551.8	13.1		98.4	24.97	0.16

Notes:
Isotopic ratios corrected for blank, radioactive decay, and mass discrimination, not corrected for interferring reactions. Ages calculated ralative to FC-1 Fish Canyon Tuff sanidine interlaboratory standard at 27.84 Ma. Errors quoted for individual analyses include analytical error only, without interferring reaction or J uncertainties. Integrated age calculated by recombining isotopic measurements of all steps. Integrated age error calculated by recombining errors of isotopic measurements of all steps. Plateau age is inverse-variance-weighted mean of selected steps. Plateau age error is inverse-variance-weighted mean error (Taylor, 1982) times root MSWD where MSWD>1. Plateau and integrated ages incorporate uncertainties in interferring reaction corrections and J factors. Decay constants and isotopic abundances after Steiger and Jaeger (1977).
symbol preceding sample ID denotes analyses excluded from plateau age calculations. Discrimination = 1.00743 ± 0.00124
Correction factors:
$(^{39}Ar/^{37}Ar)_{Ca}$ = 0.0007 ± 2e-05
$(^{36}Ar/^{37}Ar)_{Ca}$ = 0.00028 ± 5e-06
$(^{38}Ar/^{39}Ar)_{K}$ = 0.01077
$(^{40}Ar/^{39}Ar)_{K}$ = 0.0002 ± 0.0003